Insights into the Structure and Self-Assembly of Organic-Semiconductor/Quantum-Dot Blends

Daniel T. W. Toolan,* Michael P. Weir,* Jesse Allardice, Joel A. Smith, Simon A. Dowland, Jurjen Winkel, James Xiao, Zhilong Zhang, Victor Gray, Adam L. Washington, Anthony J. Petty II, John E. Anthony, Neil C. Greenham, Richard H. Friend, Akshay Rao, Richard A. L. Jones, and Anthony J. Ryan

Controlling the dispersibility of crystalline inorganic quantum dots (QD) within organic-QD nanocomposite films is critical for a wide range of optoelectronic devices. A promising way to control nanoscale structure in these nanocomposites is via the use of appropriate organic ligands on the QD, which help to compatibilize them with the organic host, both electronically and structurally. Here, using combined small-angle X-ray and neutron scattering, the authors demonstrate and quantify the incorporation of such a compatibilizing, electronically active, organic semiconductor ligand species into the native oleic acid ligand envelope of lead sulphide, QDs, and how this ligand loading may be easily controlled. Further more, in situ grazing incidence wide/small angle X-ray scattering demonstrate how QD ligand surface chemistry has a pronounced effect on the self-assembly of the nanocomposite film in terms of both small-molecule crystallization and QD dispersion versus ordering/aggregation. The approach demonstrated here shows the important role which the degree of incorporation of an active ligand, closely related in chemical structure to the host small-molecule organic matrix, plays in both the self-assembly of the QD and small-molecule components and in determining the final optoelectronic properties of the system.

1. Introduction

Nanocomposite films containing quantum dots (QDs) have attracted considerable attention due to their wide application in solar cells,[1] light-emitting diodes,[2] photodetectors, photon-upconversion, and recently, photon-multipliers.[8] In these applications, ligands bound to the QD surface not only determine QD dispersibility in the surrounding (host) material, but also influence both the electronic and optical properties.

Often, QD ligands (e.g., oleic acid (OA), trioctylphosphine oxide) inhibit electronic coupling between the host material and the QD. Efficient electron coupling between the host material and QDs may be achieved through ligand exchange approaches with short ligands (e.g., pyridine, butylamine, and hexanoic acid) or approaches to remove the QD ligands

D. T. W. Toolan, A. J. Ryan
Department of Chemistry
The University of Sheffield
Dainton Building, Brook Hill, Sheffield S3 7HF, UK
E-mail: d.toolan@sheffield.ac.uk

M. P. Weir, J. A. Smith, R. A. L. Jones
Department of Physics and Astronomy
The University of Sheffield
Hicks Building, Hounsfield Road, Sheffield S3 7RH, UK
E-mail: Michael.Weir@nottingham.ac.uk, weir.mp@gmail.com

M. P. Weir
School of Physics and Astronomy
University of Nottingham
Nottingham NG7 2RD, UK

J. Allardice, S. A. Dowland, J. Winkel, J. Xiao, Z. Zhang, V. Gray, N. C. Greenham, R. H. Friend, A. Rao
Cavendish Laboratory
Cambridge University
J. J. Thomson Avenue, Cambridge CB3 0HE, UK

J. A. Smith
Department of Physics
Clarendon Laboratory
Oxford University
Oxford, OX1 3PU, UK

V. Gray
Department of Chemistry – Ångström Laboratory
Uppsala University
Box 523, Uppsala 751 20, Sweden

A. L. Washington
ISIS Pulsed Neutron and Muon Source
STFC Rutherford Appleton Laboratory
Didcot OX11 0QX, UK

A. J. Petty II, J. E. Anthony
University of Kentucky Center for Applied Energy Research
2582 Research Park Drive, Lexington, KY 40511, USA

R. A. L. Jones
Department of Materials
John Owens Building
The University of Manchester
Oxford Road, Manchester M13 9PL, UK

(e.g., thermal annealing).[3] A further approach has been the in situ synthesis of QDs inside the host material, without stabilizing organic ligands.[4] However, such approaches often generate phase-segregated QD morphologies.[4,5]

An alternative approach is the employment of ligands that are chemically compatible with the host material, and thus have a tendency for mixing with it. Such an approach has been demonstrated for a QD:polymer nanocomposite, where grafting block copolymers to QDs enabled their effective dispersion in a bulk polymer matrix (albeit at relatively low QD loadings of 2.5 wt%).[6] Recently, well-dispersed QDs have been achieved in a phenylethylammonium (PEA) perovskite:QD hybrid system, through performing a QD ligand exchange with a PEA hydrobromide salt. Thus, the functionalized QDs have an increased solubility in the perovskite precursor solution and trigger fast perovskite nucleation to achieve homogeneous incorporation of QDs in the perovskite matrix without detrimental QD aggregation.[7] Such studies demonstrate that surface engineering approaches can be employed as a route for suppressing QD aggregation/phase segregation in nanocomposite QD films.

In a small-molecule:QD nanocomposite, we have recently demonstrated significantly improved QD dispersibility (compared to native OA QD ligands) through modifying the PbS QD surface with an active, highly soluble semiconductor ligand [6,11-bis((triisopropylsilyl)ethynyl)tetracene-2-carboxylic acid (TET-CA)], which in turn allows for the QDs to be incorporated in a blend with a matched organic semiconductor 5,12-bis((triisopropylsilyl)ethynyl)tetracene.[8] These systems are of particular interest for their potential as singlet fission photon multiplication materials (SF-PM). This highly promising technology has the potential to enable PV technologies to surpass the Shockley–Queisser limit, through converting high energy (blue) photons and re-emitting multiple lower energy (red) photons better energetically matched to the photovoltaic bandgap and therefore minimize thermalization losses.[9]

In this work, we use TIPS-Tc:(PbS-TET-CA) as a model system to study the incorporation of electronically-active ligands (in this case, TET-CA) into the native OA ligand shell of PbS QDs and to determine how the degree of incorporation can be controlled. We then use in situ X-ray scattering measurements to explore the impact of the QD surface functionalization with active ligands on the dispersibility of QDs within the organic semiconductor host and the corresponding effect on the crystallization of the organic semiconductor matrix itself. Our data provide real time insights into the complex self-assembly phenomena and nanoscale structure formation within organic-QD nanocomposites and pave the way for the rational design of ligand exchange protocols and solution processing conditions in order to obtain optimal nanocomposite morphologies for optoelectronic applications.

2. Results and Discussion

2.1. Solution Small Angle Neutron and X-Ray Scattering

PbS QDs synthesized with native OA ligands (PbS-OA) were exchanged with TET-CA to obtain TET-CA ligated PbS QDs (PbS-TET-CA). The OA to TET-CA ligand exchange was con-

trolled by employing QD:ligand mass ratios of 1:0.1 and 1:0.25, with the aim of achieving QDs with either a low degree of TET-CA ligand incorporation (PbS-C1) or a high degree of TET-CA ligand incorporation (PbS-C2) onto the PbS QD core. The efficacy of this approach was investigated via tandem small-angle X-ray and neutron scattering measurements (SAXS and SANS, respectively) on solutions of PbS-OA and the various TET-CA ligand exchanged QDs (PbS-C1 and PbS-C2) in order to quantify structural changes in the QD ligand shell. Using a method similar to one previously described,[10] SAXS contrast was utilized to measure the radius and polydispersity of the QD cores from solutions in toluene, while SANS with isotopic contrast provided by deuterated toluene revealed the structure of the OA/TET-CA ligand shell. For all SANS fitting, the radius and polydispersity of the QD derived from SAXS data were used as a constraint to the model (see Experimental Section).

The as-synthesized PbS-OA QDs were found via SAXS to have PbS cores measuring 22 Å in radius with a lognormal polydispersity of 0.1, suggesting a standard deviation of 2.2 Å in the QD core radius. The SANS data showed changes in the ligand shell scattering composition and thickness (**Figure 1**b,c, respectively). The ligand shells became more packed with ligand upon exchange, as the competitive adsorption of TET-CA reduced the overall amount of solvent present in the ligand shells (22% d-toluene in the shell for native PbS-OA versus 4% d-toluene in the shell for exchanged species PbS-C1 and PbS-C2), consistent with increasing TET-CA coverage on the QD after exchange. Optical absorption measurements of the original OA capped QDs reveal an exciton peak at 1170 nm (Figure S5, Supporting Information), suggesting a core radius of 20 Å, in good agreement with the SAXS measurements.

Compared with the OA capped QDs, the absorption of the ligand exchanged QDs also has sharp absorption features around 540 nm indicating the presence of TET-CA ligands (Figure S4, Supporting Information). The coverage of ligands was determined based on the molar absorption coefficient of TET-CA (determined to be 22 500 $M^{-1}cm^{-1}$ in toluene) and the molar absorption of PbS QDs with a core diameter of 40 Å, estimated from the empirical formula determined by Moreels et al. (for further details see Supporting Information).[11] The ligand coverages of PbS-C1 and PbS-C2 were calculated to be 0.41 ± 0.05 and 0.53 ± 0.05 TET-CA per nm^2 from the absorption measurements. The optical measurements were consistent with the conclusions from the SANS measurements, although the former method has a significantly lower associated uncertainty. The results indicate increased ligand shell densities for the PbS-OA → PbS-C1 → PbS-C2 exchange series. The number of TET-CA ligands per nm^2 (Figure 1d) and the total number of TET-CA ligands per QD core (Figure 1e), increases for the higher stoichiometry (PbS-C2) in accordance with predictions. For clarity and to make reference to the measured ligand coverages we will now denote PbS-C1 and PbS-C2 as PbS-(0.41) TET-CA and PbS-(0.53)TET-CA, respectively.

An important finding here is that for both PbS-(0.41)TET-CA and PbS-(0.53)TET-CA samples, a significant amount of OA is still present in the ligand shell as illustrated in Figure 1f, either chemisorbed or physisorbed to the QDs. This is consistent with our previous observations that greater-than-monolayer OA coverage is typical for the PbS-OA QDs synthesized by our
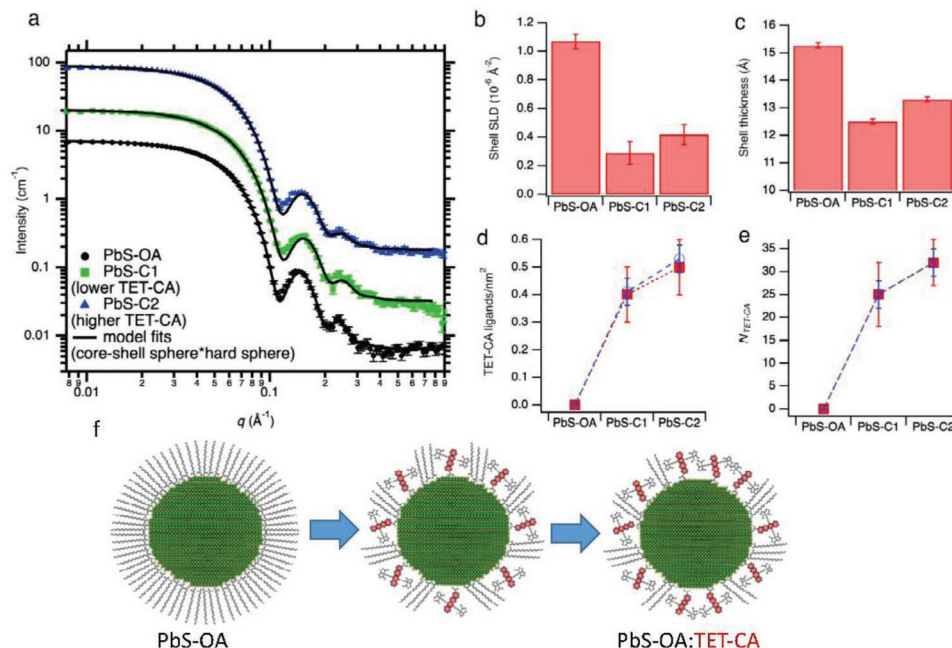
Figure 1. Structural study of the ligand coverage in solutions of PbS-OA QDs and increasing coverages of TET-CA ligand. a) SANS data from the LOQ small-angle diffractometer (ISIS, Rutherford Appleton Laboratory) and the associated fits (solid black lines) using a core-shell sphere×hard-sphere model, PbS-OA (black circles) data at calibrated intensity, and PbS-TET-CA [PbS-C1 (green squares) and PbS-C2 (blue squares)] data scaled for clarity. Data derived from the fits to the SANS data, showing b) the neutron scattering length density, c) the ligand shell thickness, and d) an estimate of coverage in units of ligands per nm² of the TET-CA ligand on the PbS surface as a function of QD type from optical absorption (blue circles) and from SANS (red squares) and e) the number of TET-CA ligands per QD corresponding to part (d). f) Illustration showing the PbS-OA QDs with increasing coverages of TET-CA ligand.

methods.[10] Thus, ligand exchange to active ligands does not completely remove the native ligands, with those which remain continuing to play an important role both electronically and structurally. For a full description of the SANS fitting and subsequent coverage calculations, see the Supporting Information.

2.2. Grazing Incidence Wide Angle X-Ray Scattering

To gain insights into how QD ligand chemistries and ligand coverage affect the self-assembly of TIPS-Tc:QD blends (with respect to: i) QD ordering and ii) TIPS-Tc crystalline morphologies), in situ grazing incidence wide-angle X-ray scattering (GIWAXS) measurements were performed during drop-casting of TIPS-Tc:QD blends at a mass ratio of 10:1. The experiments were performed on TIPS-Tc:QD blends (with PbS QDs possessing either -OA/(0.41)TET-CA/(0.53)TET-CA ligands) drop-cast from toluene on silicon substrates heated to 50 °C. Before considering the role of TET-CA ligand coverage on the self-assembly process of the TIPS-Tc:QD blends, it is first convenient to describe the QD morphologies of final as-cast films, and critically, how these relate to SF-PM device performance.

For the TIPS-Tc:QD blends, scattering features at low q (0.05–0.3 Å^{-1}) arise from the QD component of the blend. **Figure 2**a shows the radially integrated grazing incidence X-ray scattering data from TIPS-Tc:PbS-[OA, (0.41)TET-CA and (0.53)TET-CA] films after drying, representing the final QD morphologies in the films. A model was fitted to the data comprising a spherical form factor with a hard-sphere structure factor that describes scattering from QDs still distributed with liquid-like

order within the film, in addition to a face-centered-cubic paracrystal (colloidal crystal with optional packing disorder parameter) contribution to take into account regions of the film where the QDs are close-packed into a colloidal crystal. This sphere×hard-sphere+FCC paracrystal model is separated into its component parts in Figure 2b,c, which shows the contributions to the model for TIPS-Tc:PbS-(0.41)TET-CA (Figure 2b), that is, a final structure where there are significant proportions of QDs in sphere×hard-sphere or FCC paracrystal arrangements, and for TIPS-Tc:PbS-(0.53)TET-CA (Figure 2c), that is, a final structure where QDs are mostly arranged in the sphere×hard-sphere (dispersed) arrangement. A rough estimate of the volume fraction of scattering material in either structure (e.g., proportional to the number of QDs) is obtained from a limited-range calculation (i.e., performed on only the experimental q-range without extrapolation) of the scattering invariant $Q^*_{limited} = \int_{q_{min}}^{q_{max}} q^2 I(q) \, dq$ for each of the model components. These estimates are presented in **Table 1** and show the extent to which native PbS-OA and PbS-(0.41)TET-CA QDs form aggregated, packed morphologies. Increased TET-CA functionalization of the QD significantly promotes QD dispersion within the film, with >90% of QDs well-dispersed with liquid-like order for the TIPS-Tc:PbS-(0.53) TET-CA.

The TIPS-Tc:(PbS-TET-CA) system provides an excellent test-bed to study the effect of sample nanostructure upon optoelectronic performance, via its photon multiplication process. In this process, high energy photons absorbed by the organic host (here TIPS-Tc) undergo singlet fission to convert the photogenerated spin-0 singlet exciton into spin-1 triplet
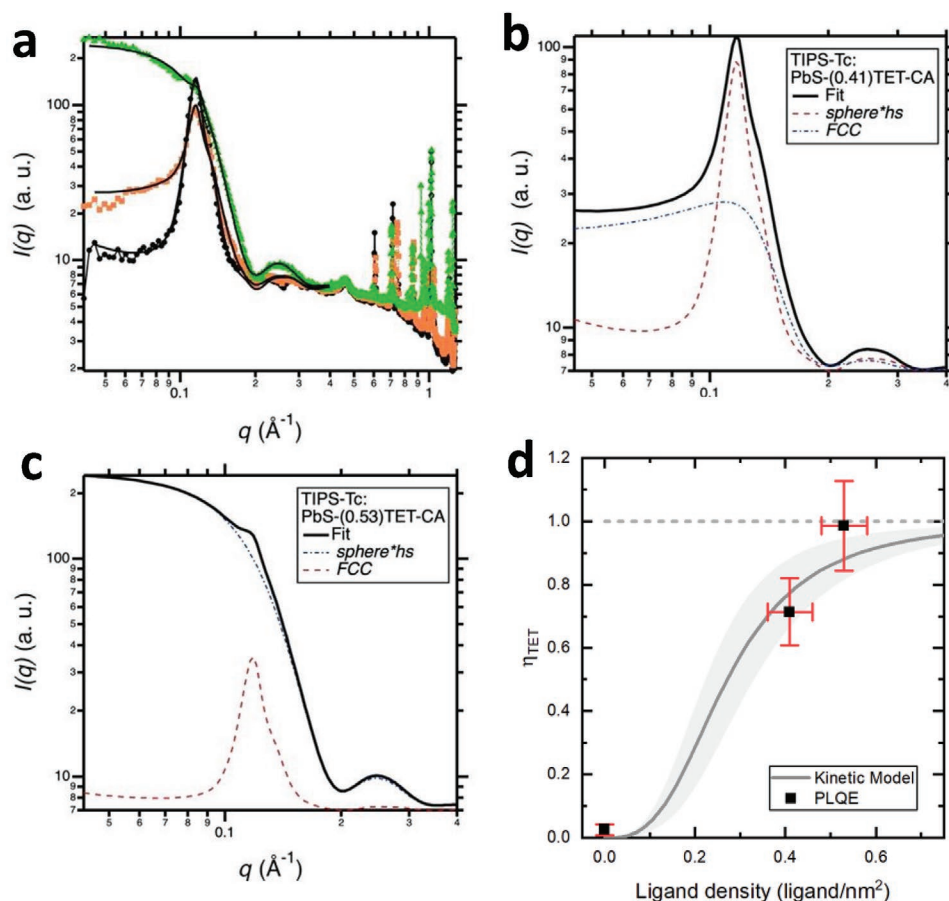
Figure 2. Grazing incidence X-ray scattering of final morphologies of TIPS-Tc:QD drop-cast films, a) GIWAXS scattering patterns of the final structures of TIPS-Tc:PbS-OA (black circles), TIPS-Tc:PbS-(0.41)TET-CA (orange squares), and TIPS-Tc:PbS-(0.53)TET-CA (green triangles) films, with associated fits (solid black lines) to the low q region of the scattering signal (comprising information on quantum dot length scales) employing a sphere×hard-sphere + FCC paracrystal model. Illustration of the components of the model as applied to the data for b) the TIPS-Tc:PbS-(0.41)TET-CA and c) TIPS-Tc:PbS-(0.53) TET-CA blend films, that is, an illustration of the relative contributions from QDs distributed as sphere×hard-sphere (dot-dashed blue line) and FCC (dashed red line), and the combined model (solid black line). d) Triplet transfer efficiency as a function the TET-CA ligand density of the QDs within the TIPS-Tc:PbS films (10:1 mass ratio). The triplet transfer efficiency for TIPS-Tc:PbS-OA, TIPS-Tc:PbS-(0.41)TET-CA, and TIPS-Tc:PbS-(0.53)TET-CA films measured using IR PLQE data (black squares). Error bars taking into account the propagation of uncertainty in the singlet fission efficiency of TIPS-Tc and the uncertainty in the ligand density. The calculated triplet transfer efficiency in the large aggregated domain limit ($\frac{r_{Dom}}{r_{QD}} \gg \sqrt{\frac{D}{r_{QD}k}} \approx 10$), using a TET-CA ligand density dependant triplet transfer velocity of $k_{lig} = 3.1 \pm 0.3$ nm³ µs⁻¹ per ligand (grey curve). Calibration between ligand density and the fraction of dispersed QDs was achieved using a coefficient of $\Omega = 3.1 \pm 0.2$ (nm² per ligand)². Uncertainty bounds calculated based on the propagation of uncertainty from the triplet transfer and triplet decay rate (light grey area).

Table 1. Table showing the integrated relative volume fractions of sphere×hard-sphere (denoted sphere*hs) and FCC ordered QDs, PLQE of the QDs (658 nm) and the SF-PM (515 nm), the exciton multiplication factor ($\eta_{SF} \times \eta_{TET}$) and resulting triplet transfer efficiency (η_{TET}) assuming a singlet fission yield of $\eta_{SF} \approx 180\%$.

Sample (TET-CA ligands per nm²)	ϕ sphere*hs	ϕ FCC	PLQE (SF-PM) [%]	PLQE (QD) [%]	$\eta_{SF} \times \eta_{TET}$ [%]	η_{TET} [%]
PbS-OA (0)	0.03	0.97	4.5 ± 0.2	23.5 ± 2.8	4.5 ± 2.9	2.5 ± 1.6
PbS-(0.41) TET-CA	0.44	0.56	18.0 ± 0.9	14.5 ± 1.7	129 ± 19	71 ± 11
PbS-(0.53) TET-CA	0.93	0.07	23.5 ± 1.2	14.2 ±1.7	177 ± 25	99 ± 14

excitons. These excitons then diffuse through the TIPS-Tc domains and encounter the PbS-TET-CA. The triplets then transfer from TIPS-Tc to the TET-CA ligands and then into the PbS QDs. Here the excitons can recombine radiatively, emitting NIR photons. Ideally the system would convert each high energy photon absorbed into two NIR photons, thus giving a photoluminescence quantum efficiency (PLQE) of 200%. The ideal nanostructure to achieve this would involve QDs dispersed through the film with no QD aggregation (as aggregation reduces the QD PLQE) and with the distances between the QDs commensurate with the triplet exciton diffusion length in TIPS-Tc.

The photon multiplication (SF-PM) performance was monitored by the QD PLQE enhancement when exciting the TIPS-Tc singlet fission host (515 nm, SF-PM), compared to direct

excitation of the PbS QDs (658 nm, QD) (employing previously described methods).[8] From the PLQE enhancement, the relative absorption of the SF-PM components and assuming a 180% singlet fission yield (η_{SF}),[12] the exciton multiplication factor η_{EMF}, and triplet transfer efficiency ($\eta_{TET} = \eta_{EMF}/\eta_{SF}$) were calculated. Figure 2d and Table 1 show that there is a positive correlation between the observed triplet transfer efficiency and the TET-CA ligand density on the surface of the PbS QDs.

Kinetic modeling is employed to understand the relationship between the effect of TET-CA ligand density on the observed SF-PM performance, via a model that separates triplet exciton acceptor sites into either dispersed QDs or aggregated QD domains. The triplet transfer efficiency was calculated as a function of the fraction of QDs dispersed within the TIPS-Tc SF-host material and the TET-CA ligand density on the PbS QDs (see Supporting Information for details). The model takes into account previously observed triplet transfer and decay rates, triplet exciton diffusion within the TIPS-Tc, a finite triplet transfer velocity from TIPS-Tc to the QDs, and the mass composition of the SF-PM components used to produce the films. Of particular note, we calculate that a triplet transfer velocity of $k = 1.6 \pm 0.1$ nm µs^{-1} (at a TET-CA ligand density of 0.53 ligand per nm^2) is necessary to combine the previously determined triplet transfer rate and our best estimate of the TIPS-Tc triplet diffusion coefficient (based on values for TIPS-Pentacene).[8,13] Comparison to the magnitude of the triplet diffusion coefficient (D) and the QD radius (r_{QD}), this triplet transfer velocity indicates that the SF-PM system is kinetically limited ($k \ll D/r_{QD}$), rather than purely limited by the diffusion of triplets to the QDs.[14] We find that inclusion of a ligand density dependent triplet transfer velocity, with coefficient $k_{lig} = 3.1 \pm 0.3$ nm^{3}µs^{-1} per ligand, results in an improved agreement between calculated triplet transfer efficiencies and the measured PLQE values (Figure S3b, Supporting Information). This ligand dependant velocity quantifies how the TET-CA ligand mediates triplet transfer while the intrinsic OA ligands do not.[15,16]

We illustrate the adverse effect of large aggregated QDs domains on the SF-PM performance (Figure S1, Supporting Information). In particular, for the limit of large QD aggregated domains, where the domain diameter is much greater than ≈ 10 times the QD radii ($r_{Dom}/r_{QD} \gg \sqrt{D/r_{QD}k} \approx 10$), the triplet transfer efficiency is limited by the fraction of dispersed QDs within the film (Figures S1,S4, Supporting Information).

Figure 2d shows the consistency, within uncertainty, of the triplet transfer efficiencies determined by PLQE measurements with those calculated using kinetic modeling for arbitrarily large QD aggregate domains. If a finite QD domain size is used, we find that aggregate domains with radii of at least $r_{Dom} \approx 140$ nm (domains which are at least ≈ 40 QDs in diameter) are required for agreements with the PLQE values (see Supporting Information for full details). It is interesting that whilst the kinetic modeling suggests that aggregate domains must possess radii of at least 140 nm, the measured values obtained from the GIWAXS data are of the order of ≈ 40 nm. We ascribe the discrepancy between these two values to combinations of the following factors: i) GIWAXS data only accounting for the overall size of the highly ordered aggregates and not taking into account any disordered boundaries or roughness of the surrounding aggregate

domains and ii) due to the simplifications in the theoretical methods used in the kinetic model. We find that application of this kinetic model is consistent with the observed trend in triplet transfer efficiency with TET-CA ligand coverage and, critically, highlights the importance of the TET-CA ligand not only to facilitate the dispersion of the QDs within the SF-host but also to enable the triplet transfer into the QDs. As previously shown, an additional benefit of the increased dispersion of the QDs is the reduction of aggregation-assisted PL quenching in the QDs.[8]

The low q scattering data for the final TIPS-Tc:QD films clearly demonstrate that the nature of the ligand shells has a dramatic effect on the self-assembled QD morphologies that form during drop-casting. **Figures 3–5** present in situ GIWAXS data for the TIPS-Tc:QD blends in order to resolve links between the various components of the self-assembly process, namely: TIPS-Tc crystallization (Figure 3) and QD ordering (Figure 4 for TIPS-Tc:PbS-OA & TIPS-Tc:PbS-(0.41)TET-CA, and Figure 5 for TIPS-Tc:PbS-(0.53)TET-CA).

For drop-cast TIPS-Tc, in the absence of QDs, in situ 2D scattering patterns (Figure 3a) and radially integrated scattering data (Figure 3d) show the formation of sharp, well-defined, isotropic scattering rings at $q > 0.5$ Å^{-1} after 3 min of drying. The presence of a significant number of Bragg diffraction peaks within the Debye–Scherrer rings indicates that the evolving crystalline morphology consists of many large domains of randomly oriented crystallites. Comparison of the drop-cast TIPS-Tc with powder diffraction data [Cambridge Crystallographic Data Centre (CCDC) deposition: 962 667 (top pane)] (Figure 3d) indicates that the drop cast TIPS-Tc reported here forms the same crystalline lattice as reported previously. The radially integrated in situ scattering data reveal an additional transient peak at $q = 0.92$ Å^{-1} at 3 and 4 min, which is not present in the final film. The presence of such scattering features indicates that TIPS-Tc may form an intermediate, short-lived, and metastable phase during crystallization from solution.

For the TIPS-Tc:PbS-OA blend (Figures 3a,4a and insets), the onset of crystallization (defined as the appearance of TIPS-Tc crystal peaks at $q > 0.5$ Å^{-1}) occurred at a later time (≈ 4 min) than for neat TIPS-Tc. The addition of PbS-OA does not appear to have a dramatic effect on how TIPS-Tc films crystallize, with all of the expected reflections predicted from bulk TIPS-Tc present. Interestingly, the transient scattering feature at 0.92 Å^{-1}, observed for native TIPS-Tc and potentially indicative of a metastable crystalline state, is not observed at any point during the drop-casting of the TIPS-Tc:PbS-OA blend.

For the TIPS-Tc:PbS-OA blend, at time (t) = 1 min, the low q QD scattering features are consistent with those observed in the earlier solution SANS/SAXS measurements (Figure 1a), where QDs may be described as non-interacting quasi-spherical objects. As solvent evaporation proceeds, contributions from the structure factor increasingly dominate the low q scattering and as TIPS-Tc:QD concentrations increase the QDs begin to interact. At $t = 2$ min, "Bragg rods" are observed in the 2D scattering pattern, indicative of lateral ordering of PbS-OA QDs at the substrate/solution interface. As drying proceeds further, the Bragg rod features evolve into strong diffraction spots, commensurate with FCC scattering, in addition to the formation of
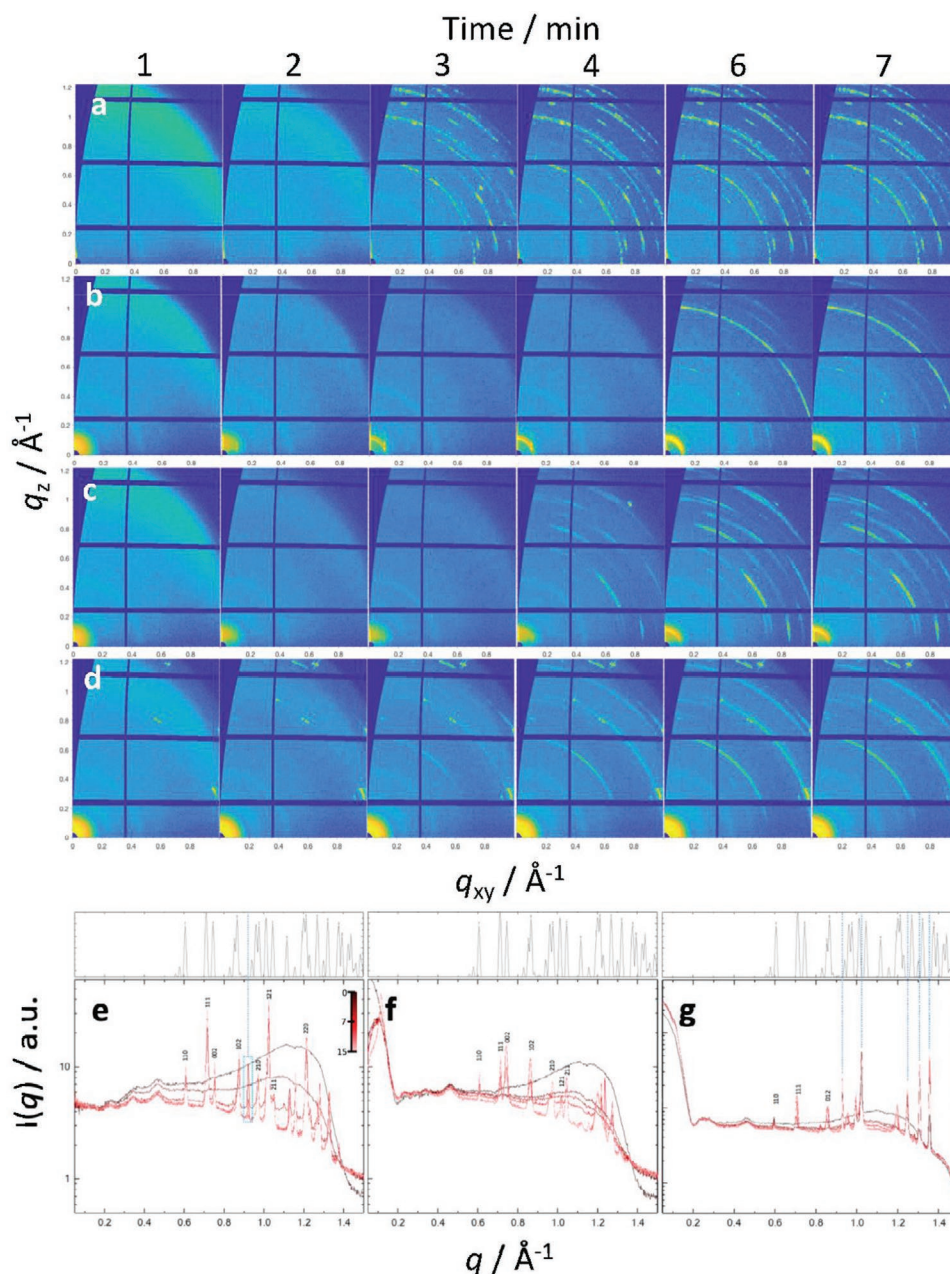
Figure 3. In situ grazing incidence X-ray scattering showing effect of QD ligand on the crystallization of TIPS-Tc for drop-cast TIPS-Tc:QD blends with 2D scattering patterns presented at 60 s intervals showing the evolution of TIPS-Tc crystalline structure for: a) TIPS-Tc, b) TIPS-Tc:PbS-OA, c) PbS-(0.41)TET-CA, and d) PbS-(0.53)TET-CA. Corresponding radially integrated scattering data are presented for e) TIPS-Tc, f) TIPS-Tc:PbS-OA, and g) PbS-(0.53)TET-CA, (with the top panels showing the X-ray diffraction patterns for bulk TIPS-Tc from CCD deposition 962 667).

scattering rings whose positions are well described by an FCC structure factor (the evolution of QD FCC structural features is discussed in detail later in this section). The presence of well-defined Bragg-rod FCC features in tandem with the radial FCC features indicates the co-existence of FCC-ordered QDs at the substrate-film interface in coexistence with QD FCC crystals randomly oriented within the bulk of the crystalline TIPS-Tc matrix. Interestingly, QD ordering occurs at earlier times than for the crystallization of neat TIPS-Tc, with the addition of PbS-OA QDs leading to the delayed onset of TIPS-Tc crystal-

lization. We therefore attribute this behavior to two causes: i) that the addition of a significant proportion of QDs to the TIPS-Tc solution leads to slower evaporation rates; and ii) that despite individual PbS-OA QDs having the potential to act as nucleation sites for TIPS-Tc crystallization, their unfavorable surface chemistry prohibits this. However, as the onset of QD ordering occurs before TIPS-Tc crystallization in the TIPS-Tc:PbS-OA blend, it is likely that the formation of larger scale QD aggregates (comprising many QDs) act as heterogenous nucleation sites to initialize the TIPS-Tc crystallization.
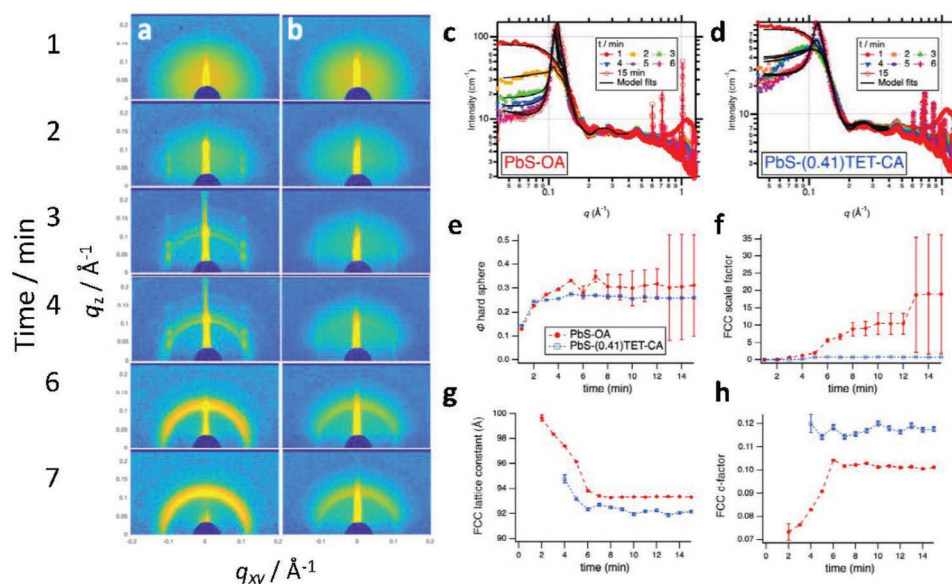
**ADVANCED
SCIENCE NEWS**

www.advancedsciencenews.com

**ADVANCED
FUNCTIONAL
MATERIALS**

www.afm-journal.de

Figure 4. In situ grazing incidence X-ray scattering QD morphological development for drop-cast TIPS-Tc:PbS-OA and TIPS-Tc:PbS-(0.41)TET-CA, showing 2D scattering patterns at 60 s intervals focusing on QD ordering (q = 0.035–0.35 Å^{-1}), for: a) TIPS-Tc:PbS-OA and b) TIPS-Tc:PbS-(0.41)TET-CA. Corresponding radially integrated scattering data are shown for c) TIPS-Tc:PbS-OA and d) TIPS-Tc:PbS-(0.41)TET-CA with associated fits using the sphere×hard-sphere + FCC paracrystal model. Parameters extracted from fit data as a function of drying time are shown in: e) the hard-sphere volume fraction; f) the scale factor of the FCC peaks; g) the lattice constant of the FCC structure; and h) the disorder parameter ("d-factor") of the FCC QD structure.

For the TIPS-Tc:PbS-(0.41)TET-CA blend, where the PbS QDs possess a small degree of TET-CA incorporation, the in situ GIWAXS data reveal that morphological development (Figures 3b,d,4b,e) progresses very similarly to that of the TIPS-Tc:PbS-OA blend, in terms of both TIPS-Tc crystallization and QD ordering. However, in comparison with PbS-OA, the initial Bragg rod type features present from t = 2 min are not as prevalent, nor is the FCC structure factor that arises from QD colloidal crystal type features. As such, three potential QD arrangements may be ascribed to the TIPS-Tc:PbS-(0.41)TET-CA film, namely: i) FCC-ordered QDs at the substrate-film interface, ii) FCC-ordered QD crystals randomly orientated within the bulk of the crystalline film, and iii) randomly distributed,

dispersed QDs within the TIPS-Tc matrix, with inter-particle correlations described by a hard-sphere structure factor.

The evolution of the QD assembly structure for the TIPS-Tc:PbS-OA and TIPS-Tc:PbS-(0.41)TET-CA is explored in more detail in Figure 4c–h, were the sphere×hard-sphere + FCC paracrystal model fits the main features of the radially integrated data as the both the PbS-OA and PbS-(0.41)TET-CA QDs develop from the initial liquid-like order of the as-cast solution through to the dried film morphology. The various parameters extracted from the model for PbS-OA and PbS(0.41)-TET-CA are shown in Figure 4e–h. The hard-sphere volume fraction (Figure 4e) increases with drying time as solvent leaves the film. Meanwhile, the scale factor of the FCC paracrystal
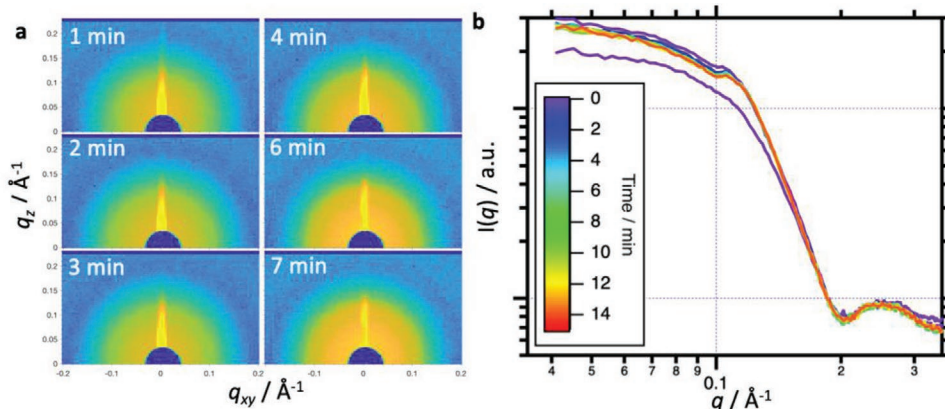

Figure 5. In situ grazing incidence X-ray scattering QD morphological development for drop-cast TIPS-Tc:PbS-(0.53)TET-CA showing a) 2D scattering patterns at 60 s intervals focusing on QD ordering (q = 0.035–0.35 Å^{-1}) and b) corresponding radially integrated scattering data.

scattering component (Figure 4f) also increases as the QDs pack within parts of the drying film. Where the FCC scale factor is non-zero, the lattice constant (Figure 4g) and the paracrystal disorder parameter (Figure 4h) are extracted (note that for in situ GIWAXS performed on a drying film it is not possible to calibrate scattering on an absolute intensity scale, and so an arbitrary overall scale factor is used, whilst only the relative intensities of scattering contributions have physical meaning).

As the TET-CA ligand loading is increased further, that is, in the TIPS-Tc:PbS-(0.53)TET-CA film, the morphological behavior deviates significantly from that which was observed for both the TIPS-TC:PbS-OA and TIPS-Tc:PbS-(0.41)TET-CA blend films and is shown in Figure 5. For the TIPS-Tc:PbS-(0.53) TET-CA film, crystalline TIPS-Tc features become apparent in the first minute of film formation, at $t = 1$ min. The low-q scattering contributions from the PbS-(0.53)TET-CA QDs largely resemble those of the sphere×hard-sphere arrangement indicative of well-dispersed QD that is present for the majority of the drop-casting process. However, it should be noted that at $q = 0.125$ Å^{-1}, there is a clear deviation from the aforementioned model. Whilst this scattering feature is weak, it becomes more prevalent as the film dries and is attributed to the formation of a small proportion of FCC-ordered QD crystals as observed for the PbS-(0.41)TET-CA film, albeit at a significantly lower volume fraction (ϕ_{FCC} of 0.07 compared with 0.56 for QDs with 0.53 and 0.41 TET-CA ligands per nm^2, respectively). The crystalline ordering of the TIPS-Tc component of the blend film is also markedly different to that observed for native TIPS-Tc, with five crystalline peaks ($q = 0.92$, 1.02, 1.25, 1.31, and 1.35 Å^{-1}) that cannot be ascribed to the reflections originating from TIPS-Tc with the space group $P\ 2_1\ 2_1\ 2_1$ (as listed for CCDC deposition 962 667) and which comprise a significant proportion of the scattering. The scattering data therefore indicate that the presence PbS-(0.53)TET-CA QDs may promote the formation of an alternative crystalline polymorph to that observed for bulk crystalline TIPS-Tc.

The dramatic changes in TIPS-Tc structure, both in the onset of crystallization and in the crystalline morphology, for the TIPS-Tc:PbS-(0.53)TET-CA blend film, indicates that the PbS-(0.53)TET-CA QDs act as strong nucleating agents, which also significantly promotes the formation of the crystalline polymorph observed for the crystallization of neat TIPS-Tc. Unlike for the native-TIPS-Tc, where polymorphism is short-lived, in the TIPS-Tc:PbS-(0.53)TET-CA blend the polymorph remains as the dominant crystalline morphology.

3. Conclusion

In summary, we have demonstrated and quantified how the incorporation of an "active" ligand species into the ligand envelope of PbS QDs may be easily controlled. Further, we demonstrate how QD ligand surface chemistry has a pronounced effect on how TIPS-Tc:QD films self-assemble in terms of both small molecule crystallization and QD dispersion versus ordering/aggregation. For the TIPS-Tc:(PbS-OA/-(0.41)TET-CA) blends, QD ordering occurs prior to TIPS-Tc crystallization and a significant proportion of the QDs exist in aggregated colloidal crystal morphologies. However, for the TIPS-Tc:PbS-(0.53) TET-CA blends, little QD ordering is observed, with QDs

remaining largely dispersed for the entirety of the film formation process and TIPS-Tc crystallization. This work highlights the importance of the TET-CA ligand to not only facilitate the dispersion of the QDs within the SF-host but also enable the triplet transfer into the QDs, as demonstrated via kinetic modeling of PLQE data. This work demonstrates the key role which active ligands play in the final structures of QD:organic semiconductor nanocomposites. In this work, the active ligands are deliberately selected to be closely related to the host smallmolecule organic semiconductor matrix, and therefore to compatibilize QD and matrix both chemically and energetically. In this way, the degree of incorporation of the active ligand in the QD shell not only determines the function of the nanoparticle itself but also exerts critical control upon the final nanocomposite structure, to complete the functional material. This approach demonstrates the rational design of SF-PM systems by tailoring the composition of QD ligand shells in order to determine the final structural and optoelectronic properties of each film.

4. Experimental Section

Quantum Dot Synthesis: The synthesis of PbS-OA QDs was carried out following modified versions of previously reported methods.[17] Briefly, lead oxide (0.45 g), OA (7 g), and 1-octadecene (10 g) were loaded in a three-neck flask and degassed at 110 °C for 2 h. Subsequently, the reaction flask was flushed with nitrogen and the temperature was lowered to 95 °C. A solution containing bis(trimethylsilyl)sulphide (210 μL) in 1-octadecene (5 mL) was rapidly injected into the lead precursor solution. The reaction flask was then allowed to cool down naturally to ambient temperature (≈25 °C). The PbS-OA QDs were first extracted by adding hexane and acetone, followed by centrifugation. The QDs were further purified with hexane and acetone and then re-dispersed in toluene at a concentration of ≈100 mg mL^{-1}. The dispersion was filtered with a 0.45 um PTFE syringe filter before ligand exchange.

Exchange of PbS-OA to Varying PbS-TET-CA Coverages: The ligand exchange process was performed in a nitrogen filled glovebox. The PbS-OA QDs were first diluted to a concentration of 20 mg mL^{-1}. The TET-CA ligand solution (100 mg mL^{-1} dissolved in tetrahydrofuran, THF) was then added into the QD dispersion, with a QD:ligand mass ratio of 1:0.1 and 1:0.25 for PbS-C1 and PbS-C2, respectively. As TET-CA has poor solubility in toluene, extra THF was added to the mixture to prevent precipitation of the ligands (toluene:THF = 4:1). The mixture was stirred for 30 min. The exchanged QDs were then purified with toluene/acetone by centrifugation. Finally, the QDs were re-dispersed in toluene for film fabrication and characterization.

Small-Angle X-Ray Scattering: Samples were dispersed in toluene at 5 mg mL^{-1} in small quantities (≈100 μL) to conserve material, and injected into borosilicate glass capillaries with external diameter 2 mm and a nominal wall thickness of 0.01 mm. SAXS data were measured on a Xeuss 2.0 instrument equipped with an Excillum MetalJet liquid gallium source. Scattering patterns of the samples as well as toluene and empty capillary backgrounds were collected for 900 s. Silver behenate and glassy carbon standards were also measured to provide camera length and intensity calibrations, respectively. Sample SAXS data were radially integrated as a function of $q = 4\pi\sin\theta/\lambda$ and corrected for the appropriate adjustments and backgrounds (transmission, capillary and solvent background, time, thickness, and absolute intensity). Data were fitted in the SasView software package[18] using a core-shell-sphere form factor, to account for the high-electron-density PbS cores and the organic ligand coatings that were effectively spherical in shape[10] and a hard-sphere structure factor to account for the liquid-like correlation of the QD centers in the solution. The structure factor produces a small but significant correction to the data at these concentrations. The master PbS-OA quantum dot batch used in this study was found to

have a radius 22.2 Å with a lognormal polydispersity of 0.1, suggesting a standard deviation of 2.2 Å.

Small-Angle Neutron Scattering: SANS was carried out on the LOQ[19] small-angle diffractometer at the ISIS Pulsed Neutron Source (STFC Rutherford Appleton Laboratory, Didcot, U.K.). Samples were prepared in deuterated solvents or blends of hydrogenous and deuterated solvents, providing the necessary contrast and were contained in 1 or 2 mm path length quartz cells (Hellma GmbH), with the longer path length reserved for fully deuterated solvents and the shorter path length required to reduce the absorbance and incoherent background in h/d solvent blends. Sample solutions of a desired concentration were prepared through drying aliquots of stock solutions of PbS-OA under nitrogen, followed by the addition of the relevant solvent (d-toluene or h/d-toluene blend). LOQ is a fixed-geometry time-of-flight instrument which utilizes neutrons with wavelengths between 2.2 and 10 Å. Data were simultaneously recorded on two, 2D, position-sensitive, neutron detectors, to provide a simultaneous q-range of 0.007–0.46 Å^{-1}. The beam diameter was collimated to 12 mm at the sample. For all collected data, each raw scattering data set was corrected for the detector efficiencies, sample transmission, and background scattering and converted to scattering cross section data ($\partial\Sigma/\partial\Omega$ vs q) using the Mantid framework (version 3.13.0).[20] These data were placed on an absolute scale (cm^{-1}) using the scattering from a standard sample (a solid blend of hydrogenous and perdeuterated polystyrene) in accordance with established procedures.[21]

SANS fitting was performed using the SasView software package.[18] The SANS curves for PbS-OA, PBS-C1 (low TET-CA coverage, PbS-(0.41)TET-CA), and PBS-C2 (high TET-CA coverage, PbS-(0.53)TET-CA) fitted with the core-shell-sphere model with a hard-sphere structure factor (Figure 1a), using the parameters obtained from SAXS to constrain the PbS core radius and lognormal polydispersity to 22.2 and 2.2 Å, respectively. The key parameters of interest extracted from the fits were the shell neutron scattering length density and the shell thickness (Figure 1b,c), which together describe the dimensions and molecular composition of the shell in the following way. The coherent neutron scattering length density of each pure molecular component is the sum of the coherent scattering lengths b_n of each of the n atoms (thereby accounting for both the number and species of atoms) in the molecule divided by the molecular volume, that is,

$$\rho = \frac{1}{V_m}\sum_n b_n \tag{1}$$

In this way, using the molecular volume in the bulk material gave the neutron SLD at bulk density. Neutron scattering lengths are well tabulated[22] and the NIST Neutron activation and scattering calculator is a useful online tool to perform the entire calculation from simple input parameters.[23] The neutron scattering length density ρ of a system with i component materials was simply derived from the volume fractions of the various components multiplied by the individual values of ρ measured or estimated for the component materials at bulk densities, that is,

$$\rho = \sum_i \phi_i \rho_i \tag{2}$$

For the as-synthesized dots, covered in OA, and measured in the solution phase, the shell SLD was governed by the degree of penetration of the solvent and is therefore given by

$$\rho = \phi_{OA}\,\rho_{OA} + \phi_{solvent}\rho_{solvent} \tag{3}$$

Furthermore, in the case of exchange to a novel ligand from a starting batch of OA-ligated QDs, the shell SLD was governed by the coverage of the new ligand, the residual OA that was not removed during exchange, and the solvent penetration into the new composite ligand layer, that is,

$$\rho = \phi_{ligand}\rho_{ligand} + \phi_{OA}\,\rho_{OA} + \phi_{solvent}\rho_{solvent} \tag{4}$$

This approach treats the ligand shell as a homogenous mixture of its chemical components with a given thickness. It does not resolve individual ligand molecules, so any structural information must be inferred from the shell thickness, for example, in order to determine whether ligand molecules are lying flat or extended from the quantum dot surface. Further discussion of this method was previously published[10] making reference to other useful techniques and studies[24] which extracted further information from quasi-spherical quantum dot scattering.

Estimation of Monolayer Coverage from SAXS/SANS Scattering Length Densities: A simple estimate of a full monolayer coverage of TET-CA could be obtained by projecting the quasi-spherical surface area of the QD onto a flat surface. This ensured that the monolayer estimate contained only material that could conceivably be attached to the QD surface, not a misleading shell of crystalline TET-CA. This surface area gave a volume of the TET-CA monolayer at $4\pi r^2 h$ where r is the QD radius and h is an estimate of the height of a single ligand molecule. The volume of the annular spherical shell $\frac{4}{3}\pi[(r+h)^3 - r^3]$ was greater than the simple projected volume $4\pi r^2 h$ by a factor $\frac{h^2}{3r^2}+\frac{h}{r}+1$, having a value of 1.52 for the typical parameters used in the current study. A value of h may be estimated given that the carboxylic acid group is on one of the tetracene carbons furthest from the TIPS groups in TET-CA. Using $r = 22$ Å, $h = 10$ Å, and $\rho_{TET-CA} = 1.1$ g.cm^{-3} gave a total of 65 TET-CA molecules in a full monolayer (molecular weight TET-CA 633.02 g mol^{-1}). The annular shell this monolayer occupied was therefore part-filled with solvent molecules and was only 65% filled by one complete monolayer. These considerations also shed some light on the displacement of OA by the much larger TET-CA ligand, giving an area per molecule of 95.6 Å^2 for TET-CA compared with 28.5 Å^2 for OA, suggesting a successful TET-CA attachment displaces at least 3 OA ligands.

Steady-State Absorption: A Shimadzu UV3600Plus spectrometer was used to measure the absorbance spectra of the solutions in 1 mm quartz cuvettes.

PLQE Measurements: The integrating sphere and PLQE measurement procedure was described previously.[16,25] In summary, an integrating sphere with a Spectralon-coated interior (Newport 819C-SL-5.3) was used for the absolute measurement. 515 and 658 nm laser diodes (Thorlabs) with a beam diameter at the sample of 3 mm was used as the excitation source. Light from the sphere was coupled into an Andor Kymera 328i Spectrograph equipped with an InGaAs detector (Andor, iDus InGaAs 490). A NIST certified calibration lamp from Newport, 200 W Quartz Tungsten Halogen Lamp driven by an OPS-Q250 power supply, was used to generate a photons/count calibration file.

In Situ GISAXS/GIWAXS Studies of PbS-OA/TET-CA Ligand Density Series Self-Assembly with TIPS-Tc: In situ grazing incidence small-angle X-ray scattering (GISAXS)/GIWAXS was performed on the Xeuss instrument equipped with an Excillum MetalJet liquid gallium X-ray source ($\lambda = 9.243$ Å). Alignment was performed on silicon substrates via three iterative height (z) and rocking curve (Ω) scans, with the final grazing incidence angle set to $\Omega = 0.2°$. Scattering patterns were recorded on a vertically-offset Pilatus 1M detector with a sample to detector distance of 559 mm, calibrated using a silver behenate standard to achieve a q-range of 0.045–1.2 Å^{-1}. Scattering data were collected using collimating slits of 0.5×0.6 mm ("high flux" mode), giving a direct beam of ≈ 2 mm^2. 2D images were recorded on the detector every 60 s after the deposition of a droplet of 50 µL of TIPS-Tc (200 mg mL^{-1}):QD (20 mg mL^{-1}) in toluene. The images were masked to remove the sample horizon, detector module gaps, and beamstop and radially integrated from the apparent beam center. Data correction and reduction were performed using the GIXSGUI MATLAB toolbox.[26] 2D scattering data were reduced to 1D via radial integration, which was performed with a mask to remove contributions from "hot pixels," the substrate horizon, and reflected beam. Fitting was performed using the SasView software package.[18]

Supporting Information

Acknowledgements

Conflict of Interest

The authors declare no conflict of interest.

Data Availability Statement

The data that support the findings of this study are available from the corresponding author upon reasonable request.

Keywords

[1] a) O. O. Matvienko, Y. N. Savin, A. S. Kryzhanovska, O. M. Vovk, M. V. Dobrotvorska, N. V. Pogorelova, V. V. Vashchenko, *Thin Solid Films* **2013**, *537*, 226; b) M. Helgesen, R. Søndergaard, F. C. Krebs, *J. Mater. Chem.* **2010**, *20*, 36; c) N. Zhao, T. P. Osedach, L.-Y. Chang, S. M. Geyer, D. Wanger, M. T. Binda, A. C. Arango, M. G. Bawendi, V. Bulovic, *ACS Nano* **2010**, *4*, 3743; d) A. J. Moulé, L. Chang, C. Thambidurai, R. Vidu, P. Stroeve, *J. Mater. Chem.* **2012**, *22*, 2351.

[2] a) S. Coe, W.-K. Woo, M. Bawendi, V. Bulović, *Nature* **2002**, *420*, 800; b) M. Zorn, W. K. Bae, J. Kwak, H. Lee, C. Lee, R. Zentel, K. Char, *ACS Nano* **2009**, *3*, 1063.

[3] a) N. C. Greenham, X. Peng, A. P. Alivisatos, *Phys. Rev. B* **1996**, *54*, 17628; b) J. D. Olson, G. P. Gray, S. A. Carter, *Sol. Energy Mater. Sol. Cells* **2009**, *93*, 519; c) Y. Zhou, F. S. Riehle, Y. Yuan, H.-F. Schleiermacher, M. Niggemann, G. A. Urban, M. Krüger, *Appl. Phys. Lett.* **2010**, *96*, 013304.

[4] E. Martínez-Ferrero, J. Albero, E. Palomares, *J. Phys. Chem. Lett.* **2010**, *1*, 3039.

[5] a) A. Watt, E. Thomsen, P. Meredith, H. Rubinsztein-Dunlop, *Chem. Commun.* **2004**, 2334; b) H. C. Leventis, S. P. King, A. Sudlow, M. S. Hill, K. C. Molloy, S. A. Haque, *Nano Lett.* **2010**, *10*, 1253.

[6] J. Kwak, W. K. Bae, M. Zorn, H. Woo, H. Yoon, J. Lim, S. W. Kang, S. Weber, H.-J. Butt, R. Zentel, S. Lee, K. Char, C. Lee, *Adv. Mater.* **2009**, *21*, 5022.

[7] L. Gao, L. N. Quan, F. P. García de Arquer, Y. Zhao, R. Munir, A. Proppe, R. Quintero-Bermudez, C. Zou, Z. Yang, M. I. Saidaminov, O. Voznyy, S. Kinge, Z. Lu, S. O. Kelley, A. Amassian, J. Tang, E. H. Sargent, *Nat. Photonics* **2020**, *14*, 227.

[8] J. Allardice, V. Gray, S. Dowland, D. T. W. Toolan, M. P. Weir, J. Xiao, Z. Zhang, J. F. Winkel, A. Petty, J. Anthony, R. Friend, A. J. Ryan, R. A. L. Jones, N. Greenham, A. Rao, arXiv:2009.05764 **2020**.

[9] a) A. Rao, R. H. Friend, *Nat. Rev. Mater.* **2017**, *2*, 17063; b) M. J. Y. Tayebjee, A. Rao, T. W. Schmidt, *J. Photonics Energy* **2018**, *8*, 022007.

[10] M. P. Weir, D. T. W. Toolan, R. C. Kilbride, N. J. W. Penfold, A. L. Washington, S. M. King, J. Xiao, Z. Zhang, V. Gray, S. Dowland, J. Winkel, N. C. Greenham, R. H. Friend, A. Rao, A. J. Ryan, R. A. L. Jones, *J. Phys. Chem. Lett.* **2019**, *10*, 4713.

[11] I. Moreels, K. Lambert, D. Smeets, D. De Muynck, T. Nollet, J. C. Martins, F. Vanhaecke, A. Vantomme, C. Delerue, G. Allan, Z. Hens, *ACS Nano* **2009**, *3*, 3023.

[12] H. L. Stern, A. Cheminal, S. R. Yost, K. Broch, S. L. Bayliss, K. Chen, M. Tabachnyk, K. Thorley, N. Greenham, J. M. Hodgkiss, J. Anthony, M. Head-Gordon, A. J. Musser, A. Rao, R. H. Friend, *Nat. Chem.* **2017**, *9*, 1205.

[13] N. A. Pace, N. V. Korovina, T. T. Clikeman, S. Holliday, D. B. Granger, G. M. Carroll, S. U. Nanayakkara, J. E. Anthony, I. McCulloch, S. H. Strauss, O. V. Boltalina, J. C. Johnson, G. Rumbles, O. G. Reid, *Nat. Chem.* **2020**, *12*, 63.

[14] a) F. C. Collins, G. E. Kimball, *J. Colloid Sci.* **1949**, *4*, 425; b) K. Schulten, *PHYCS 498NSM: Theoretical Biophysics - Chapter 8 - Rates of Diffusion-Controlled Reactions*, **1999**, https://www.ks.uiuc.edu/Services/Class/PHYS498/LectureNotes/chp8.pdf (accessed: October 2018).

[15] K. E. Knowles, M. Malicki, E. A. Weiss, *J. Am. Chem. Soc.* **2012**, *134*, 12470.

[16] J. R. Allardice, A. Thampi, S. Dowland, J. Xiao, V. Gray, Z. Zhang, P. Budden, A. J. Petty, N. J. L. K. Davis, N. C. Greenham, J. E. Anthony, A. Rao, *J. Am. Chem. Soc.* **2019**, *141*, 12907.

[17] M. A. Hines, G. D. Scholes, *Adv. Mater.* **2003**, *15*, 1844.

[18] SasView Home Page, http://www.sasview.org (accessed: September 2020).

[19] R. Heenan, J. Penfold, S. King, *J. Appl. Crystallogr.* **1997**, *30*, 1140.

[20] Mantid Project Home Page, http://www.mantidproject.org/ (accessed: September 2020).

[21] G. T. Wignall, F. Bates, *J. Appl. Crystallogr.* **1987**, *20*, 28.

[22] V. F. Sears, *Neutron News* **2006**, *3*, 26.

[23] NIST Neutron Activation and Scattering Calculator, https://www.ncnr.nist.gov/resources/activation/ (accessed: September 2020).

[24] a) J. Maes, N. Castro, K. De Nolf, W. Walravens, B. Abécassis, Z. Hens, *Chem. Mater.* **2018**, *30*, 3952; b) S. W. Winslow, Y. Liu, J. W. Swan, W. A. Tisdale, *ACS Mater. Lett.* **2019**, *1*, 209; c) S. W. Winslow, W. Shcherbakov-Wu, Y. Liu, W. A. Tisdale, J. W. Swan, *J. Chem. Phys.* **2019**, *150*, 244702.

[25] J. C. de Mello, H. F. Wittmann, R. H. Friend, *Adv. Mater.* **1997**, *9*, 230.

[26] Z. Jiang, *J. Appl. Crystallogr.* **2015**, *48*, 917.